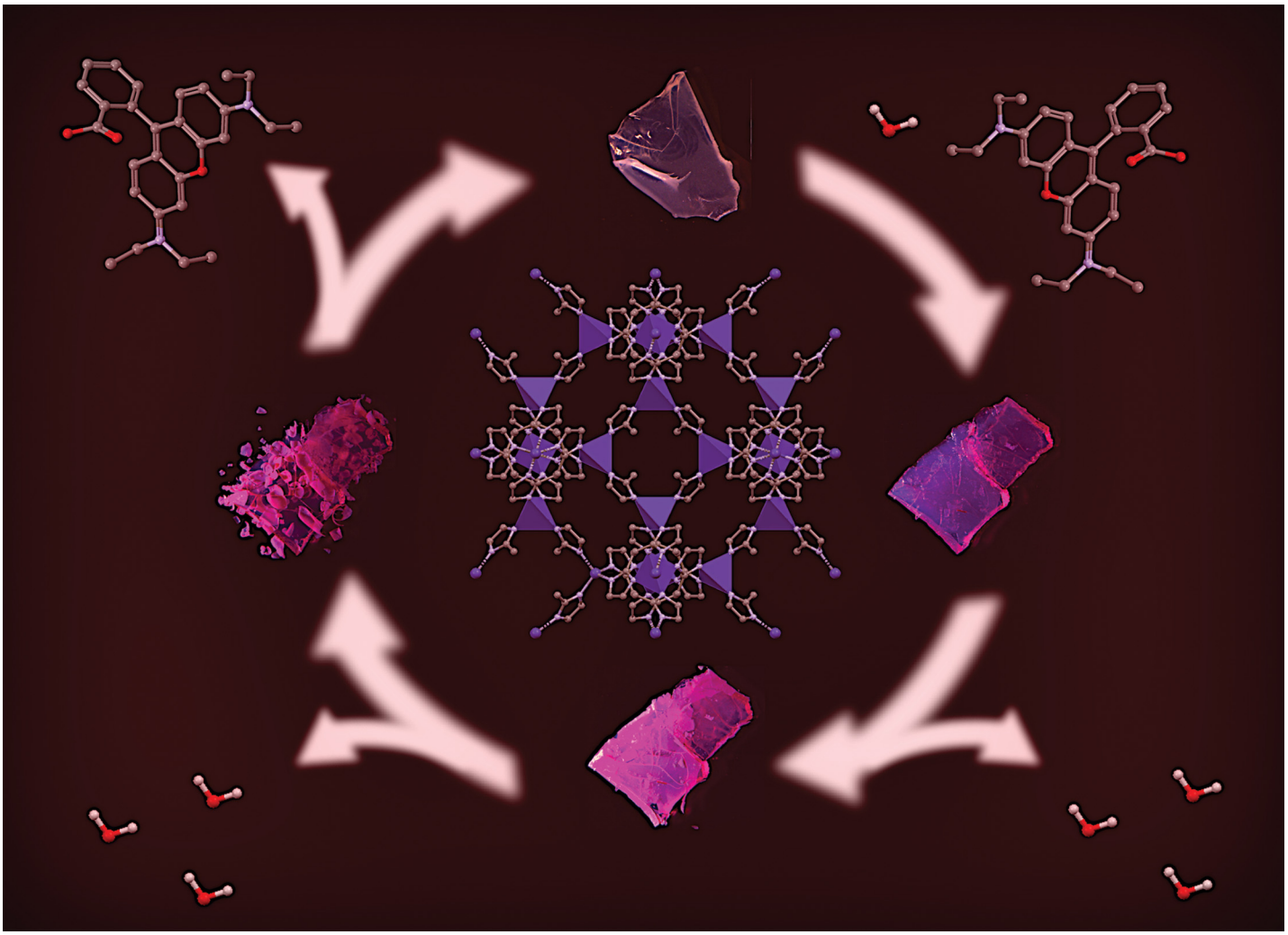

Showcasing research from Dr Jose de Jesus Velazquez-Garcia and collaborators, FS-SCS, Deutsches Elektronen-Synchrotron DESY, Hamburg, Germany.

Size matters: limitations of the ZIF-8 monolith and its Ni-, Co- and Cu-doped variants for the adsorption of rhodamine B

Despite its known instability in water, ZIF-8 is still used for water purification, including the adsorption of molecules significantly larger than its pore window. Here, we demonstrate that monolithic ZIF-8 and its Ni-, Co- and Cu-doped variants fail as adsorbents for rhodamine B – showing poor uptake (far below micro/nanoparticle performance) while degrading in water. The water instability causes desorption and post-drying peeling of the monoliths. This confirms that ZIF-8 monoliths are neither stable nor effective for adsorption of large molecules. These results question the suitability of ZIF-8 for water purification.

Image reproduced by permission of Jose de Jesus Velazquez-Garcia from *Mater. Adv.*, 2025, **6**, 7800.

As featured in:

See Jose de Jesus Velazquez-Garcia *et al.*, *Mater. Adv.*, 2025, **6**, 7800.

ROYAL SOCIETY OF CHEMISTRY

rsc.li/materials-advances

Registered charity number: 207890

Materials Advances

ROYAL SOCIETY OF CHEMISTRY

PAPER

View Article Online
View Journal | View Issue

Cite this: *Mater. Adv.*, 2025, **6**, 7800

Size matters: limitations of the ZIF-8 monolith and its Ni-, Co- and Cu-doped variants for the adsorption of rhodamine B

Jose de Jesus Velazquez-Garcia, *[a] Susann Frenzke, [a] Luis de los Santos Valladares, [bc] Crispin H. W. Barnes, [b] Christopher Copeman, [d] Jatinder Singh, [d] Satishkumar Kulkarni, [e] Thomas F. Keller, [ef] Henry Sanchez Cornejo, [bg] Dina Huanaco-Quispe, [h] Maryam Anwary, [i] Rachida Elorche, [i] Lina Maria Asprilla-Herrera, [j] Weronika Łukaszczyk, [k] Nuray Eroglu, [l] Dirk Eifler [l] and Simone Techert [am]

Despite numerous publications reporting the instability of ZIF-8 in water, it is still used for water purification, including the adsorption of molecules significantly larger than the pore window. This work involves the synthesis, characterisation and application of ZIF-8 monoliths, including those doped with Ni, Co and Cu at levels of 4%, 8% and 12%, for rhodamine B adsorption in water. Characterisation techniques include optical microscopy, PXRD, FTIR, SEM-EDX, TGA-FTIR and N_2 adsorption. The results reveal mm-cm sized monoliths with an identical crystalline structure and morphology, but different properties depending on the doping metal and level. Except for 4% of Co-doped ZIF-8, doping generally narrows the pore size distribution to micropores (maximum between 10.9 and 11.6 Å), whereas the undoped monolith shows a combination of micropores and mesopores (10.2–38 Å). Doping with more than 4% Co^{2+} or Cu^{2+} results in higher BET surface areas (up to 1180 and 1100 $m^2\ g^{-1}$, respectively) compared to the undoped monolith (960 $m^2\ g^{-1}$). However, when immersed in a 10 mg L^{-1} rhodamine B solution, all monoliths exhibit both slower adsorption kinetics and reduced capacities (0.61 and 1.82 mg g^{-1}) compared to the reported nano-/microsized particles. Desorption of rhodamine B occurred between 9 and 24 h, attributed to up to 20% degradation of the monolith. Immersion in Milli-Q water for five days led to a white residue on the surface, with FTIR indicating a new phase. These results suggest that ZIF-8 and its variants are unsuitable for adsorbing large molecules in water but are suitable for small molecules like gases.

Received 23rd July 2025,
Accepted 18th September 2025

DOI: 10.1039/d5ma00797f

rsc.li/materials-advances

Introduction

Metal–organic frameworks (MOFs) are porous materials that can exhibit very high surface areas and have potential for applications such as gas storage and separation, as well as catalysis.[1–3] They are composed of metal ions or clusters connected with multitopic organic linkers.[4,5] Among the various MOFs, zeolitic imidazolate framework-8 (ZIF-8) is one of the most widely used MOFs due to its simple synthesis coupled with its high thermal stability and remarkable

[a] *Deutsches Elektronen-Synchrotron DESY, Notkestr. 85, 22607 Hamburg, Germany. E-mail: jose.velazquez@desy.de*
[b] *Cavendish Laboratory, Department of Physics, University of Cambridge, CB3 0HE Cambridge, UK*
[c] *Programa de Pós-Graduação em Ciências de Materiais, Centro de Ciências Exatas e da Naturaleza, Universidade Federal de Pernambuco, 50670-901 Recife-Pe, Brazil*
[d] *Department of Chemistry and Biochemistry, Concordia University, 7141 Sherbrooke St W., Montréal, QC, Canada*
[e] *Centre for X-ray and Nano Science CXNS, Deutsches Elektronen-Synchrotron DESY, Notkestr. 85, 22607 Hamburg, Germany*
[f] *Department of Physics, University of Hamburg, 22607 Hamburg, Germany*
[g] *Laboratorio de Ceramicos y Nanomateriales, Facultad de Ciencias Fisicas, Universidad Nacional Mayor de San Marcos, 14-0149, Lima, Peru*
[h] *Escuela Académica de Ingeniería y Gestión Ambiental, Universidad Nacional Autónoma de Huanta, Jr. Manco Capac 497, Huanta, Ayacucho, Peru*
[i] *BS 06 Berufliche Schule Chemie, Biologie, Pharmazie, Agrarwirtschaft, Ladenbeker Furtweg 151, 21033 Hamburg, Germany*
[j] *Department of Chemistry, Faculty of Natural and Exact Sciences, Universidad del Valle, Calle 13 N.° 100-00, 760042 Cali, Colombia*
[k] *Faculty of Chemistry, Jagiellonian University in Kraków, Gronostajowa 2, 30-387, Kraków, Poland*
[l] *Department of Chemistry, University of Hamburg, Martin-Luther-King-Platz 6, 20146 Hamburg, Germany*
[m] *Institut für Röntgenphysik, Georg-August-Universität Göttingen, Friedrich-Hund-Platz 1, Göttingen, 37077, Germany*

chemical resistance to boiling alkaline water and organic solvents.[3,6]

ZIF-8 features sodalite (SOD) topology and consists of Zn^{2+} ions and 2-methylimidazolate (mIm) linkers in a 1 : 2 stoichiometry ratio. The framework possesses large cages (a diameter of ~11.6 Å) interconnected *via* narrow 6-ring windows (~3.4 Å). Despite the small size of the windows, ZIF-8 can adsorb molecules larger than the size of the window due to the reorientation of the imidazolate linkers enforced by guest adsorption, a phenomenon known as 'gate-opening'.[7–10]

Another intriguing feature of ZIF-8 is its ability to form monolithic structures. These monolithic MOFs are polycrystalline materials, ranging from millimetres to centimetres in size, composed of densely packed primary nanocrystals. They are particularly appealing for industrial applications since they offer an interesting combination of simple preparation and practicality, while also providing a solution to the post-synthesis processing challenges of MOFs.[11–13] Notably, ZIF-8 was the first MOF to be reported in a monolithic form, documented a decade ago.[11] Other monolithic MOFs have been reported since then, such as HKUST-1,[14] UiO-66,[15] γ-CD-MOF,[16] Zr-fumarate,[17] MIL-100(Fe), MTV-UiO-66-NH_2[18] and ZIF-67,[19] demonstrating the growing interest in this type of material.

ZIF-8 and its derivatives, whether in bulk, nanocrystal or monolithic forms, have been utilised for wastewater treatment.[20,21] For instance, Metha *et al.* employed a monolithic ZIF-8 structure embedded with tin oxide nanoparticles to achieve photocatalytic degradation of methylene blue (MB).[22] Additionally, Yang *et al.* successfully adsorbed the tetracycline antibiotic from an aqueous solution using Fe-doped ZIF-8.[23] In another study, M. Chin *et al.* studied the adsorption and photocatalytic degradation of rhodamine B (RhB) in ZIF-8 nanocrystals.[24]

Although these examples exhibit the utility of ZIF-8 and its derivatives for wastewater treatment, it is important to acknowledge its limitations. First of all, ZIF-8 is not as stable in water as originally claimed.[25] Secondly, Tran *et al.* demonstrated that large molecules, such as methyl orange and RhB, are adsorbed solely on the hydrophobic external surface of ZIF-8. In contrast, a smaller molecule, such as the cationic MB, can penetrate the micropores.[26] This suggests that ZIF-8 monoliths would exhibit lower adsorption capacities compared to nanocrystals, due to the significantly reduced ratio of external surface area to volume in monolithic structures. However, no studies have been conducted to validate this claim.

In this work, we focus on the synthesis and characterisation of monolithic ZIF-8 (ZIF-8^{mono}) alongside Co-, Ni- and Cu-doped variants (Co_xZIF-8^{mono}, Ni_xZIF-8^{mono} and Cu_xZIF-8^{mono}). Furthermore, we assess their applicability for the adsorption of RhB and their stability in water.

Experimental

Materials

Zinc nitrate hexahydrate (99%, $Zn(NO_3)_2{\cdot}6H_2O$), 2-methylimidazole (98%, $C_4H_6N_2$), nickel nitrate (99%, $Ni(NO_2)_3{\cdot}6H_2O$), copper nitrate hemi(pentahydrate) (98%, $Cu(NO_3)_2{\cdot}2.5H_2O$) and methanol (≥99.9%) were purchased from Sigma-Aldrich. Cobalt chloride hexahydrate (98%, $CoCl_2{\cdot}6H_2O$) and rhodamine B (98%, $C_{28}H_{31}ClN_2O_3$) were purchased from Alfa Aesar and Acros Organics, respectively.

Synthesis of ZIF-8 and doped ZIF-8

The synthesis of all samples was based on the procedure reported by Tian *et al.* with slight modifications.[11] In a typical synthesis procedure, 20 mmol of $Zn(NO_3)_2{\cdot}6H_2O$ was dissolved in 400 mL of methanol, while 158 mmol of 2-methylimidazole was also dissolved in 400 mL of methanol. The two solutions were then mixed and ultrasonicated for 15 min at room temperature. The resulting mixture was allowed to stand for 1 hour before undergoing centrifugation at 4200 rpm for 30 min. The resulting solid was then air-dried overnight, yielding monolith pieces of varying sizes.

For the synthesis of 4%, 8% and 12% doped monoliths, 16, 32 and 48 mL of the $Zn(NO_3)_2{\cdot}6H_2O$ solution were substituted with a 0.05 M doping solution containing either $CoCl_2{\cdot}6H_2O$, $Ni(NO_3)_2{\cdot}6H_2O$ or $Cu(NO_3)_2{\cdot}2.5H_2O$. The remaining steps of the procedure followed the established protocol for ZIF-8 monoliths. A separate document in the SI provides a detailed synthesis procedure for $Co_{8\%}$ZIF-8^{mono} using 500 mL stock solutions. Note that the typical three washing steps with methanol/ethanol following centrifugation were omitted due to difficulties in recovering the particles. It is hypothesised that higher centrifugal forces, exceeding the current equipment capabilities, are necessary to effectively recollect the particles, once they have been re-dispersed by the washing solvent.

Characterisation of monoliths

PXRD. X-ray diffraction (XRD) measurements were performed on a PXRD, KIBS Bruker D8 Discover XRD, using Cu Kα radiation (λ =1.5406 Å). The tube operating mode was set at U = 40 kV and I = 40 mA. The range of diffraction angles 2θ varied from 5° to 80° (0.01° step); the exposure per shooting point was 1 s.

FTIR. The spectra for all monolithic samples were recorded at room temperature within the wavenumber range between 400 and 4000 cm^{-1}. An Invenio-R spectrometer was used for the analysis, with samples prepared as pressed KBr pellets.

SEM/EDX. Scanning electron microscopy images were acquired and energy-dispersive X-ray analysis was performed using a dual-beam Focused Ion Beam instrument – FIB, Scios, Thermo Fischer Scientific with an accelerating voltage of 5 kV.[27]

TGA-FTIR. Thermogravimetric analysis was performed using a PerkinElmer EGA 4000. Samples were placed in alumina crucibles and subjected to heating from 30 to 600 °C, maximum temperature of the equipment using a rate of 10 °C min^{-1}. The decomposition vapours were analysed by FTIR in the wavenumber range of 400–4000 cm^{-1}. Nitrogen gas with a purity of 99.999%, flowing at a rate of 40 mL min^{-1}, was employed as the carrier gas.

N_2 gas adsorption. All monolithic samples were activated at 80 °C for 20 hours using a Micromeritics SmartVacPrep instrument equipped with a hybrid turbo vacuum pump. Nitrogen

adsorption–desorption isotherms were measured at 77 K on a Micromeritics TriStar II Plus instrument. BET surface areas were calculated using isotherm points between 0.0005 and 0.1 P/P_0. The pore size distribution was determined by non-local density functional theory (NLDFT) using a Tarazona model on cylindrical pores.

Adsorption of RhB

Adsorption experiments were carried out at room temperature. For each experiment, 100 mg of the prepared adsorbent was added to 50 mL of RhB solution with a concentration of 10 mg L^{-1}. The solution with the adsorbent was stirred for up to 96 h in the dark. To measure the UV-vis spectrum during the experiment, aliquots of approximately 250 μL were withdrawn from the flask at the following intervals: 30 min, 1, 2, 3, 4, 5, 6, 9, 24, 48, 72 and 96 h.

Due to an equipment upgrade, two spectrometers were used to collect the spectra: (1) Varian Cary-5E UV-vis-NIR spectrometer and (2) Shimadzu UV-2600i. Most of the spectra were recorded using the former, while the latter was used to measure 10% of the samples. Measurements on the Varian Cary-5e spectrometer were performed using a scan rate of 0.2 nm s^{-1} and a step size of 0.5 nm. For the Shimadzu UV-2600i, a medium scant rate (approx. 3 nm s^{-1}) and a step size of 0.5 nm were employed. Transitioning between the two devices did not result in any notable spectral differences.

Adsorption kinetics and isotherms of RhB

The adsorption capacity (Q_t) of RhB on the adsorbent was estimated based on the equation:

$$Q_t = \frac{V(C_0 - C_t)}{m} \quad (1)$$

where V is the solution volume (L), m is the adsorbent mass (g), and C_0 and C_t are concentrations (mg L^{-1}) at the beginning of the experiment and at time t, respectively. Once the adsorption capacity was calculated, the adsorption kinetics were explored based on three models: pseudo-first-order, pseudo-second-order and intraparticle diffusion.

The pseudo-first-order model is based on the Lagergren equation, which is expressed as follows:[28]

$$\log(Q_e - Q_t) = \log(Q_e) - \frac{k_1 t}{2.303} \quad (2)$$

where k_1 is the pseudo-first-order rate constant (min^{-1}), and Q_e and Q_t are the adsorption capacity (mg g^{-1}) at equilibrium and at time t (min), respectively.

In the case of the pseudo-second-order model, the following expression was used:[29–31]

$$\frac{t}{Q_t} = \frac{1}{k_2 Q_e^2} + \frac{t}{Q_e} \quad (3)$$

where k_2 is the pseudo-second-order rate constant (mg g^{-1} min^{-1}) and t, Q_e and Q_t are the same as the previous equation. The values of k_2 can be obtained from a linear plot of t/Q_t *versus* t.

Further analysis employed the Weber and Morris intra-particle diffusion model using the following equation:[24,32]

$$Q_t = k_i t^{1/2} + C \quad (4)$$

where Q_t is the adsorption capacity (mg g^{-1}) at time t (min), k_i is the intraparticle diffusion coefficient and C is a constant relevant to the boundary effect on molecular diffusion at the liquid solid interface.

Stability test

Stability tests of ZIF-8^{mono} and doped variants were conducted by adding 500 mg of the monolith into 80 mL of water in a beaker without stirring. The beaker was sealed and allowed to stand at room temperature (~20 °C) for five days. After this period, the monoliths were collected by decantation. Each partially wet monolith was then placed on a slide and left to dry under an optical microscope where images were captured.

Results

Optical microscopy, PXRD and FTIR analysis

Fig. 1 shows optical images of ZIF-8^{mono} alongside its Co-, Ni- and Cu-doped variants. The figure highlights the diversity of sizes and shapes of the monolithic pieces, as well as the distinct colours imparted by doping. The undoped ZIF-8 monolith is colourless, whereas the doped samples display unique colourations: Ni_xZIF-8^{mono} samples appear light purple, Co_xZIF-8^{mono} variants exhibit a blue-purple hue and Cu_xZIF-8^{mono} samples are dark red. Notably, the colouration becomes more intense as the dopant concentration increases.

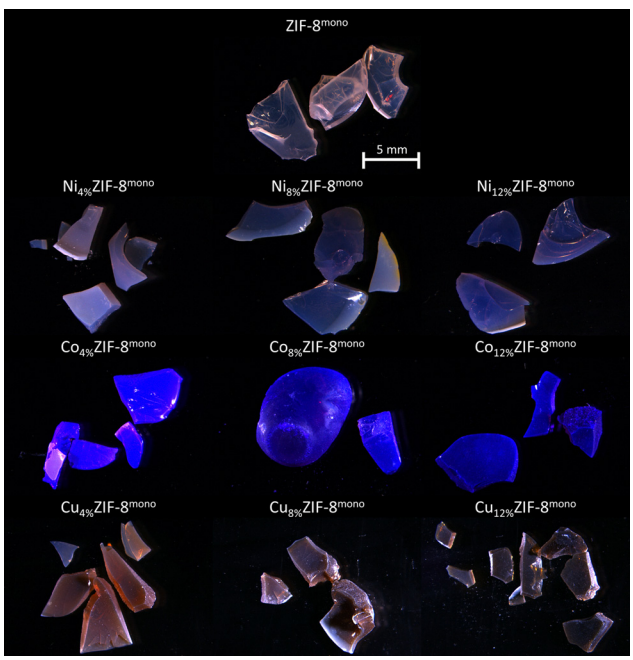

Fig. 1 Optical images of ZIF-8^{mono}, Ni_xZIF-8^{mono}, Co_xZIF-8^{mono} and Cu_xZIF-8^{mono} samples.

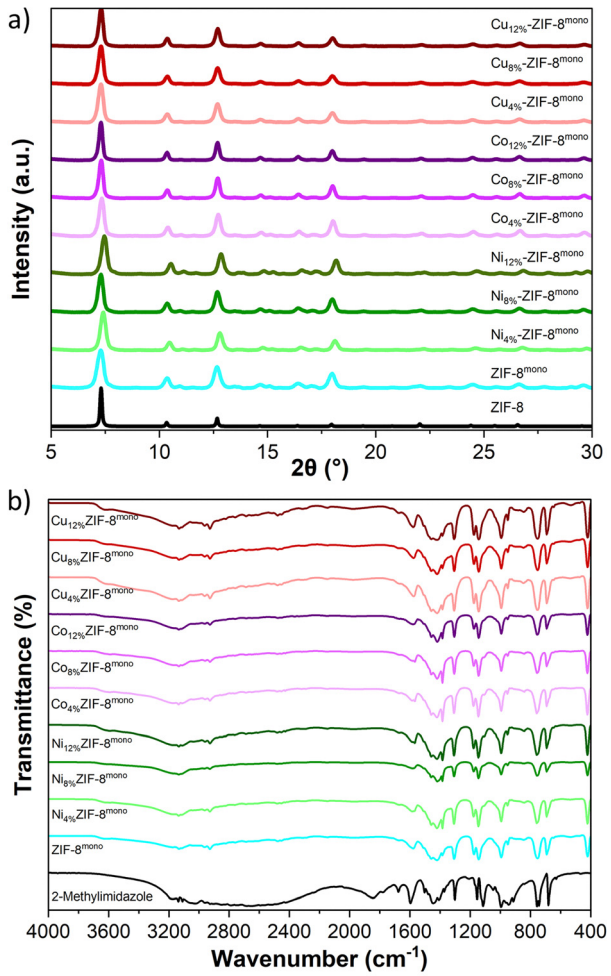

Fig. 2 (a) PXRD patterns and (b) FTIR spectra of monolithic samples, alongside the ZIF-8 simulated pattern and the 2-methylimidazole spectrum, respectively.

Fig. 2a exhibits the PXRD pattern of all monoliths. The figure demonstrates that all samples have an identical crystalline structure, closely resembling the PXRD pattern of the simulated ZIF-8. This indicates that doping ZIF-8 does not induce significant structural changes. Although a slight peak shift is observed for Ni-doped ZIF-8 monoliths, this change corresponds only to 0.2° in 2θ.

The FTIR spectra of 2-methylimidazole, ZIF-8^{mono} and its doped variants are shown in Fig. 2b, while the spectra of ZIF-8^{mono} with the value of the main peaks are presented in Fig. S1. The complete assignment of the observed bands is difficult due to the complex nature of the framework. However, Table 1 presents the preliminary assignment of most of the bands based on the study conducted by Ahmad *et al.*[33] Fig. 2b indicates that all samples are identical, displaying several bands that correspond to 2-methylimidazole. It is important to note that the presence of the band around 1583 cm^{-1} in all samples suggests the existence of defects, in particular dangling 2-methylimidazole linkers, due to the absence of M^{2+} ions.

Electron microscopy

Scanning electron miscroscopy (SEM) images of ZIF-8^{mono} and its doped variants are shown in Fig. 3. The images demonstrate that the monoliths are solid entities with flat surfaces, rather than loose agglomeration of nanoparticles, which is consistent with previous reports.[11,13,22] The elemental analysis conducted on the surface of prepared monoliths is presented in Table 2. Interestingly, the amount of nickel detected on the surface decreases as the doping amount increases. This reduction might be caused by the formation of Ni-HmIm clusters that become trapped deeper inside the monolith, providing the light-purple colour observed, as reported by Li *et al.*[34] Additionally, the amount of copper detected on the surface is significantly lower than that found in all monoliths doped with cobalt. However, the elemental mapping (Fig. S2–S11) reveals traces of the corresponding doping metals on the surface of each material.

Thermogravimetry analysis

Fig. 4 shows the TGA of all monolithic samples until 600 °C. Sharp weight losses were observed at temperatures up to 280 °C: 15% for ZIF-8^{mono}, 10–23% for Ni$_{x\%}$ZIF-8^{mono}, 8–9% for Co$_{x\%}$ZIF-8^{mono}, and 7–13% for Cu$_{x\%}$ZIF-8^{mono}. These losses are attributed to residual materials trapped within the pores. The largest weight loss that occurred in Ni$_{12\%}$-ZIF-8^{mono} is attributed to the loss of methanol molecules from the synthesis process, given that Ni-HmIm clusters strongly favour its adsorption.[34] A second weight-loss step usually takes place at around 600 °C, corresponding to the thermal degradation of the sample.[11] However, this phenomenon was not observed in

Table 1 Peak positions and assigned bands of ZIF-8^{mono} and doped variants

Peak(s)	Assigned band
3617	O–H stretching vibration of the guest water
3134	Stretching mode of C–H$_{ring}$
2928 and 2964	C–H$_{methyl}$ symmetric and asymmetric stretches
2479	–NH stretching, elongated N–H bonds due to N–H···N hydrogen bonding (defects)
1583	–CNH in-plane bending mode of dangling linker due to missing M^{2+} ions (defects)
1420 and 1458	C–H$_{methyl}$ bending
1307	Rocking mode of C–H$_{ring}$
1175	Bending modes from C–H$_{ring}$ with respect to the ring and breathing of the ring
1143	Scissoring and rocking motions of C–H$_{ring}$
994	Combination of C–H$_{methyl}$ bending and in-plane C–H$_{ring}$ rocking
420	Bending mode between the –CH$_3$ group and the imidazolate ring

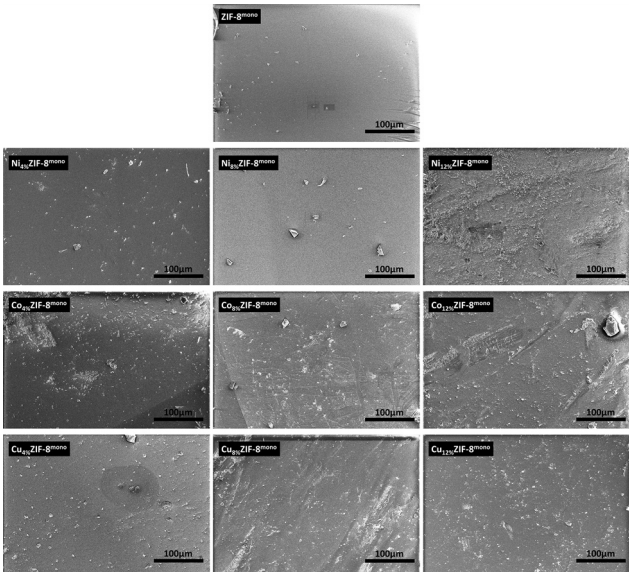

Fig. 3 SEM images of ZIF-8^{mono} and its Ni-, Co- and Cu-doped variants.

Table 2 Compositional analysis of the as-synthesised monoliths obtained by EDX

	Element (% weight)						
Material	C	N	O	Ni	Co	Cu	Zn
ZIF-8^{mono}	43.89	39.05	2.18	—	—	—	14.88
$Ni_{4\%}$ZIF-8^{mono}	44.45	33.85	3.85	0.15	—	—	17.71
$Ni_{8\%}$ZIF-8^{mono}	43.17	26.74	1.68	0.07	—	—	28.35
$Ni_{12\%}$ZIF-8^{mono}	44.09	28.69	2.19	0.00	—	—	25.02
$Co_{4\%}$ZIF-8^{mono}	44.37	38.60	2.96	—	1.03	—	13.04
$Co_{8\%}$ZIF-8^{mono}	44.87	34.81	2.64	—	2.13	—	15.55
$Co_{12\%}$ZIF-8^{mono}	44.59	29.85	1.45	—	4.48	—	19.63
$Cu_{4\%}$ZIF-8^{mono}	41.67	23.26	2.61	—	—	0.59	31.86
$Cu_{8\%}$ZIF-8^{mono}	44.18	39.38	2.38	—	—	0.37	13.68
$Cu_{12\%}$ZIF-8^{mono}	44.54	35.58	3.16	—	—	0.88	15.85

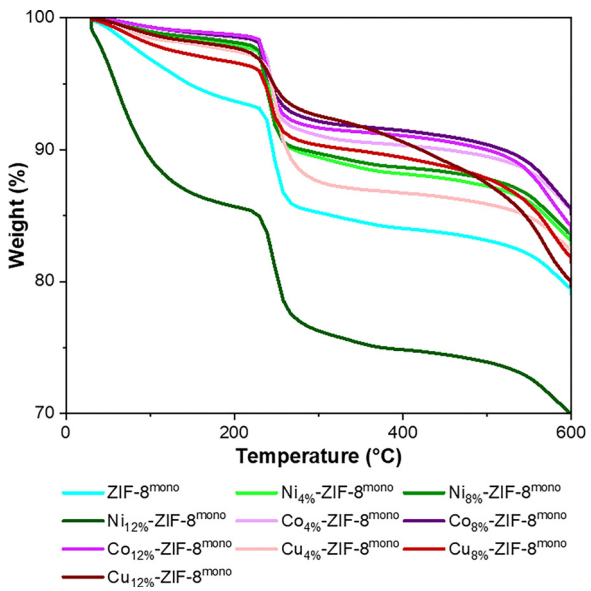

Fig. 4 Thermogravimetric analysis of ZIF-8^{mono} and its doped variants.

the present study due to equipment limitations. Nonetheless, a small shoulder was noted around 550 °C in all samples, indicating the onset of thermal degradation.

The FTIR spectra of gaseous products released at various temperatures during the TGA for all samples are presented as contour plots in Fig. S12–S15, with the empty crucible included as a reference. The presence of CO_2 peaks in the reference around 2200–2400 cm^{-1} suggests that the signals detected within this range in all samples likely originate from environmental CO_2. However, new peaks emerge in all samples around 250 °C. Fig. S16 shows the FTIR spectra of all samples at 250 °C, revealing similar peaks across all monoliths, although with varying intensities. We attribute these peaks to the emission of residual materials inside the pores, as they coincide with the sharp weight loss observed in the TGA. Importantly, these peaks were absent at the beginning (30 °C) and end (600 °C) of the experiment, as further demonstrated in Fig. S17 for ZIF-8^{mono}.

N_2 adsorption analysis

The porosity of all samples was measured using N_2 adsorption at 77 K. Table 3 summarises the main results of this analysis, while Fig. 5 and Fig. S18 show the N_2 adsorption isotherms in semi-logarithmic and linear scales, respectively. The isotherms of all the samples exhibit the typical structural flexibility and step-wise adsorption mechanism of N_2 found in ZIF-8.[7,9,10,35] The observed step in the isotherms for all samples can be attributed to the reorientation of imidazolate linkers as demonstrated by Fairen-Jimenez *et al.*[7,8] The type H2 hysteresis loop present in the isotherms of ZIF-8^{mono} and $Co_{4\%}$ZIF-8^{mono} indicates the existence of mesopores. The pore size distribution for all monoliths, shown in Fig. S19–S22 and obtained by non-local density functional theory (NLDFT), confirms that only ZIF-8^{mono} and $Co_{4\%}$ZIF-8^{mono} have a combination of micropores (10.2 Å and 15.6 Å) and mesopores (19.9 Å and 38 Å). In contrast, the other monoliths only contain micropores, ranging from 10.9 Å to 11.6 Å. Therefore, the difference observed in the isotherms of ZIF-8^{mono} and $Co_{4\%}$ZIF-8^{mono} compared to the other monoliths can be attributed to the variations in pore size. This also demonstrates that doping significantly impacts the adsorption properties of the monolith.

Table 3 Gravimetric BET area (S_{BET}), pore diameter obtained from NLDFT (D_{NLDFT}) and total pore volume (W_{total})

	S_{BET}	D_{NLDFT}	W_{total}
Material	$m^2\ g^{-1}$	Å	$cm^3\ g^{-1}$
ZIF-8^{mono}	963.58	10.2, 15.6, 19.9, 38	0.371
$Ni_{4\%}$ZIF-8^{mono}	995.27	10.9	0.361
$Ni_{8\%}$ZIF-8^{mono}	918.61	10.9	0.333
$Ni_{12\%}$ZIF-8^{mono}	975.83	10.9	0.361
$Co_{4\%}$ZIF-8^{mono}	899.39	15.6, 19.9, 38	0.341
$Co_{8\%}$ZIF-8^{mono}	1133.16	10.9	0.395
$Co_{12\%}$ZIF-8^{mono}	1178.17	11.6	0.401
$Cu_{4\%}$ZIF-8^{mono}	1059.10	10.9	0.381
$Cu_{8\%}$ZIF-8^{mono}	1099.57	10.9	0.403
$Cu_{12\%}$ZIF-8^{mono}	1041.91	10.9	0.384

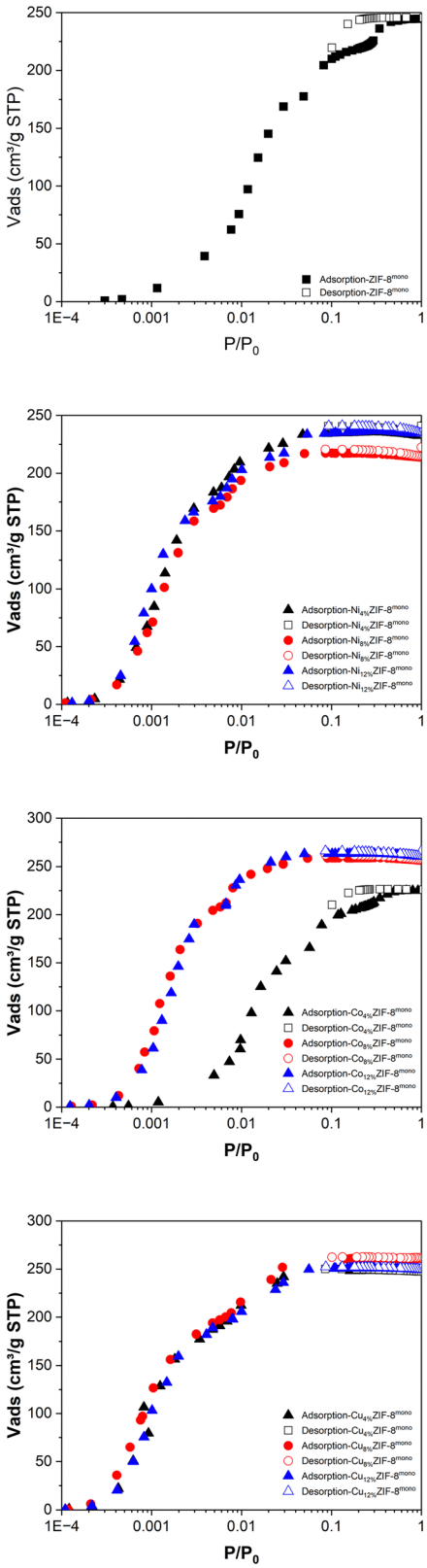

Fig. 5 Volumetric N_2 adsorption isotherms at 77 K for ZIF-8^{mono} and Ni-, Co- and Cu-doped variants.

Further analysis of the N_2 sorption properties reveals the influence of the type and amount of doping metal used. All Ni-doped monoliths and the 4% Co-doped monolith exhibit lower N_2 adsorption capacities (ranging from 224 to 235 cm^3 g^{-1}) compared to ZIF-8^{mono}, which has a capacity of 244 cm^3 g^{-1}. In contrast, the $Co_{8\%}$ZIF-8^{mono}, $Co_{12\%}$ZIF-8^{mono} and all Cu-doped monoliths possess higher adsorption capacities (between 256 and 263 cm^3 g^{-1}) than the undoped monolith. As shown in Table 3, the gravimetric BET surface areas of the Ni-doped monoliths (918–995 m^2 g^{-1}) are similar to that for ZIF-8^{mono} (963 m^2 g^{-1}). For all Cu-doped monoliths, the gravimetric BET areas (ranging from 1041 to 1099 m^2 g^{-1}) exceed those of the undoped monolith. In the case of Co-doped monoliths, the surface areas vary significantly depending on the doping amount. While $Co_{4\%}$ZIF-8^{mono} shows a lower gravimetric BET area (899 m^2 g^{-1}) than ZIF-8^{mono}, $Co_{8\%}$ZIF-8^{mono} and $Co_{12\%}$ZIF-8^{mono} exhibit higher values of 1133 and 1178 m^2 g^{-1}, respectively. It is worth noting that the gravimetric BET areas and N_2 adsorption capacities presented in the present work are slightly lower than those reported in the literature.[11,13,19,22] We attribute this discrepancy to residual linkers remaining trapped inside the pores of the monoliths, as they were not washed during the synthesis process.

Dye adsorption study

The dynamic adsorption of RhB on all monoliths is presented in Fig. 6. Note that the error bars in all graphs are relatively large; we attribute this to the difference in size of monolithic samples used in all repetitions. The figure reveals that the type and amount of dopant impact both adsorption capacity and behaviour, with reversible adsorption observed in all samples. When comparing the adsorption behaviour of all monoliths, it was observed that the undoped ZIF-8^{mono}, and the Cu- and Ni-doped variants reach maximum adsorption between 6 h and 9 h (Table 4), followed by slow desorption that takes around two days. ZIF-8^{mono}, $Ni_{4\%}$ZIF-8^{mono}, $Ni_{8\%}$ZIF-8^{mono}, $Cu_{4\%}$ZIF-8^{mono} and $Cu_{12\%}$ZIF-8^{mono} desorb over 85% of the adsorbed RhB, while $Ni_{12\%}$ZIF-8^{mono} and $Cu_{8\%}$ZIF-8^{mono} desorb under 85%. Similarly, Co_xZIF-8^{mono} samples also exhibit reversible adsorption, but their maximum is reached at 9 h for $Co_{4\%}$ZIF-8^{mono} and 24 h for the other two. Additionally, the influence of cobalt doping on the desorption behavior is notable since higher doping levels lead to a marked decrease in desorbed RhB, with $Co_{12\%}$ZIF-8^{mono} reaching only 6.8% desorption. Regarding adsorption capacities, ZIF-8^{mono} and its Ni- and Cu-variants achieved values between 0.61 and 0.98 mg g^{-1}. For Co_xZIF-8^{mono} samples, only $Co_{4\%}$ZIF-8^{mono} shows an adsorption capacity comparable with the undoped monolith, while $Co_{8\%}$ZIF-8^{mono} and $Co_{12\%}$ZIF-8^{mono} demonstrate significantly higher adsorption capacities of 1.52 and 1.82 mg g^{-1}, respectively.

The adsorption mechanism and the potential rate-controlling step were examined using three well-established kinetics models: pseudo-first-order,[28] pseudo-second-order[29–31] and intra-particle diffusion.[32] Since all samples exhibit desorption after a certain period, the kinetic models were only applied during the adsorption phase. The resulting fitting data for these models are presented in Table 5, while the plots $\log(Q_e - Q_t)$ *vs.* t, t/Q_t *vs.* t and Q_t *vs.* $t^{1/2}$ are provided in Fig. S23–S26.

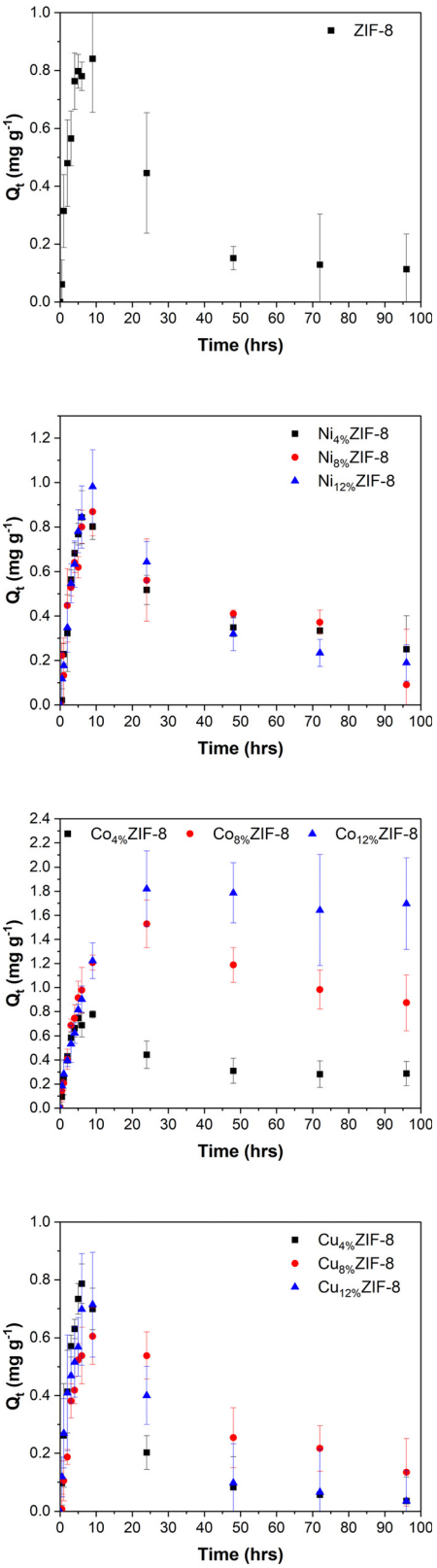

Fig. 6 Adsorption of RhB in ZIF-8^{mono} and Co-, Ni-, Cu-doped variants.

Based on the correlation constant (R^2), the pseudo-first-order kinetic model is more suitable for describing the adsorption kinetics of RhB on most of the monoliths. However, exceptions include $Co_{4\%}$ZIF-8^{mono} and $Cu_{12\%}$ZIF-8^{mono}, for which the pseudo-second-order model fits better. The rate constant for both kinetic models varies from 0.02 min^{-1} to 0.009 min^{-1} for the pseudo-first-order model and between 0.001 and 0.006 min^{-1} for the pseudo-second-order one. These values are significantly lower than those found for nano-size particles, which exhibit rate constants of k_1 = 0.1190–0.5631 min^{-1} and k_2 = 0.0685–0.5027 g mg^{-1} min^{-1}.[24] The Weber and Morris intraparticle diffusion model demonstrates that $Co_{4\%}$ZIF-8^{mono}, $Cu_{4\%}$ZIF-8^{mono} and all Ni-doped variants have only one linear region, while the others exhibit two linear regions, none of them passing through the origin. This suggests that the adsorption process of ZIF-8 monoliths involves various adsorption mechanisms.

Table 4 Adsorption of RhB in ZIF-8^{mono} and Co-, Ni- and Cu-doped variants

Sample	t_{max} h	Q_{tmax} mg g^{-1}	Desorption %
ZIF-8^{mono}	9	0.84	86.5
$Ni_{4\%}$ZIF-8^{mono}	6	0.84	70.3
$Ni_{8\%}$ZIF-8^{mono}	9	0.87	89.5
$Ni_{12\%}$ZIF-8^{mono}	9	0.98	80.7
$Co_{4\%}$ZIF-8^{mono}	9	0.78	63.0
$Co_{8\%}$ZIF-8^{mono}	24	1.53	42.9
$Co_{12\%}$ZIF-8^{mono}	24	1.82	6.8
$Cu_{4\%}$ZIF-8^{mono}	6	0.79	95.4
$Cu_{8\%}$ZIF-8^{mono}	9	0.61	77.7
$Cu_{12\%}$ZIF-8^{mono}	9	0.71	95.0

The effect of the particle size was explored by grounding the monolith and repeating the RhB adsorption experiment for 3 h. The UV-Vis spectra of the solution before and after the experiment are shown in Fig. S27. The figure demonstrates that RhB adsorption is significantly improved by the small size of the adsorbent, reaching an adsorption capacity of 3.42 (3) mg g^{-1}, which is comparable with that reported in the literature for the microcrystals (4.1 mg g^{-1}).[26] This demonstrates that the size of ZIF-8 plays a crucial role in the adsorption of RhB.

Stability of monoliths

The degradation of monoliths during the RhB adsorption test can be analysed by examining the UV-vis spectra in the ultraviolet region. Fig. S28 shows the UV-vis spectrum of the RhB solution during the adsorption test using ZIF-8^{mono}, which reveals the emergence of a band around 205 nm. The intensity of this band increases with contact time. To determine the concentration of mIm in the solution, a calibration curve ranging from 0.1 to 4 mM was established (see Fig. S29). Then, the concentration was subsequently used to calculate the percentage of degradation using the following equation:

$$\text{Degradation } (\%) = \frac{C_{mIm} V_s}{2 \cdot W_{ZIF\text{-}8} M_{ZIF\text{-}8}} \times 100 = \frac{n_{mIm}}{n_{ZIF\text{-}8}} \times 100 \quad (5)$$

Table 5 Kinetic constants and correlation coefficients

	Pseudo-first-order			Pseudo-second-order			Intraparticle diffusion		
	k_1	Q_e		k_2	Q_e		k_i	C	
Sample	min^{-1}	mg g^{-1}	R^2	g mg^{-1} min^{-1}	mg g^{-1}	R^2	g mg^{-1} $min^{-1/2}$	mg g^{-1}	R^2
ZIF-8^{mono}	0.009	0.973	0.916	0.001	1.705	0.466	0.064	−0.243	0.967
							0.009	0.623	0.834
$Ni_{4\%}$ZIF-8^{mono}	0.009	1.165	0.972	0.003	−0.652	0.210	0.061	−0.288	0.986
$Ni_{8\%}$ZIF-8^{mono}	0.006	0.939	0.870	0.002	1.416	0.658	0.042	−0.060	0.926
$Ni_{12\%}$ZIF-8^{mono}	0.006	1.148	0.980	0.001	2.079	0.900	0.053	−0.194	0.983
$Co_{4\%}$ZIF-8^{mono}	0.008	0.826	0.825	0.004	1.192	0.891	0.040	−0.029	0.894
$Co_{8\%}$ZIF-8^{mono}	0.003	1.529	0.993	0.001	1.996	0.981	0.066	−0.265	0.981
							0.027	0.511	0.957
$Co_{12\%}$ZIF-8^{mono}	0.002	1.789	0.986	0.001	2.494	0.943	0.044	−0.061	0.994
							0.048	0.018	0.983
$Cu_{4\%}$ZIF-8^{mono}	0.009	0.970	0.958	0.001	1.721	0.837	0.051	−0.148	0.990
$Cu_{8\%}$ZIF-8^{mono}	0.007	0.806	0.972	0.005	−0.351	0.162	0.036	−0.167	0.953
$Cu_{12\%}$ZIF-8^{mono}	0.008	0.916	0.783	0.006	0.971	0.972	0.052	−0.157	0.986
							0.027	0.111	0.916

where C_{mIm} is the molar concentration of mIm in solution (mmol L^{-1}), V_s is the volume of the solution (L), $W_{ZIF\text{-}8}$ is the mass of ZIF-8^{mono} or its doped variant (mg), $M_{ZIF\text{-}8}$ is the molecular mass of the ZIF-8 or its doped variant (mg $mmol^{-1}$) and n is the number of moles of mIm/ZIF-8 or its doped variant (mmol).

The degradation percentages of monoliths in relation to contact time during the RhB adsorption experiments are presented in Fig. 7. From the figure, it is evident that all monoliths experience rapid degradation within the first six hours in solutions, after which the degradation rate slows down and may plateau after approximately four days.

The extent of degradation of the adsorbent is clearly influenced by both the type and level of doping. Doping ZIF-8^{mono} with 8% of copper decreases degradation compared to the undoped monolith. In contrast, doping with 8% and 12% cobalt increases degradation. It is worth noting that $Co_{8\%}$ZIF-8^{mono} and $Co_{12\%}$ZIF-8^{mono} not only show significant degradation in water but also possess a higher adsorption capacity and lower desorption of RhB. The relation between these characteristics will be discussed in the next section.

After four days of the adsorption experiment using ZIF-8^{mono}, the RhB solution was analysed using ICP-OES. The results reveal a Zn^{2+} concentration of 1.40 mg L^{-1}, which is equivalent to just 0.24% of the metal ions presented in the added monolith. This value is significantly smaller than the 13% release suggested by the analysis of the UV-vis spectrum in the adsorption region of mIm. The discrepancy between the released mIm and the Zn^{2+} levels is quite intriguing and suggests that additional studies are needed to clarify the underlying mechanism.

Further evaluation of water stability was performed by immersing the monoliths for five days in Milli-Q water without stirring. Fig. S30 shows optical images of the monoliths after the test. The images illustrate the degradation of the external layer in all monoliths, resulting in the formation of a white powder on their surface. This residue was easily detached from the monolith by gentle shaking and then analysed by FTIR spectroscopy. Fig. 8 compares the spectrum of the original $Cu_{4\%}$ZIF-8^{mono} with that of the collected white residue. The residue's spectrum reveals four distinct peaks at 3406, 829, 514 and 478 cm^{-1}, which are not observed in the original monolith, indicating the formation of a new phase. It is plausible that the newly formed phase includes mIm, since the majority of the peaks in the new spectrum match with those found in the original monolith, where most of the peaks are assigned to linker vibrations. Notably, PXRD analysis performed on the water-immersed monoliths, including their white residue, revealed no new phases (Fig. S31). This suggests that PXRD lacks the sensitivity required to assess the water stability of ZIF-8 and its derivatives.

The white residue observed during the stability test does not appear on the surface of monoliths after RhB adsorption. Instead, these monoliths show a different behaviour: upon drying under ambient conditions, their external layer slowly peels off, as illustrated in Fig. 9 for both ZIF-8^{mono} and $Cu_{4\%}$ZIF-8^{mono}. Notably, following this peeling process, the remaining monolith retains a red colouration, indicating the presence of adsorbed RhB.

The structural and compositional integrity of the monoliths, after the water stability test and adsorption experiment, was analysed using SEM-EDX. Fig. 10 displays SEM images of the surface of $Co_{12\%}$ZIF-8^{mono} after five days in Milli-Q water and $Cu_{12\%}$ZIF-8^{mono} following RhB adsorption for four days. The corresponding elemental analysis and mapping are presented in Table 6 and Fig. S32–S33, respectively. In both the water stability test and adsorption experiment, the SEM images reveal that the monoliths developed a rougher surface compared to their pre-experiment state, suggesting surface damage. The elemental analysis and mapping indicate a lower presence of the metal atoms on the surface of $Co_{12\%}$ZIF-8^{mono} and a greater quantity of metal ions exposed on the surface of $Cu_{12\%}$ZIF-8^{mono}. These results suggest that during the adsorption of RhB, the damage caused by the water on the surface is mostly confined to the external layer, which subsequently peels off upon drying.

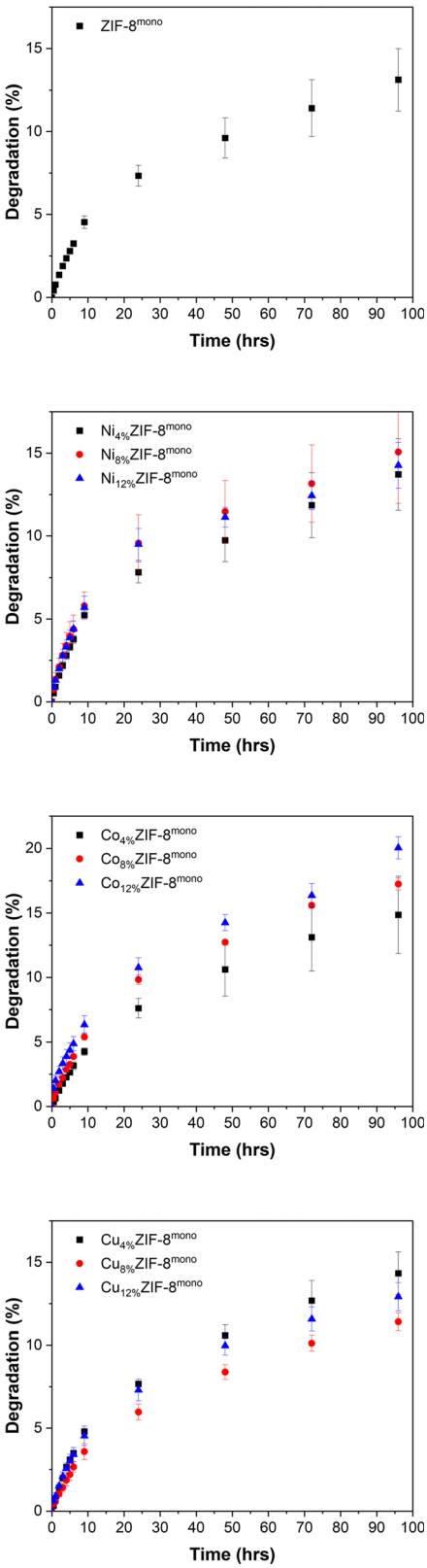

Fig. 7 Time-dependent degradation of ZIF-8^{mono} and its doped variants during RhB adsorption in aqueous solution.

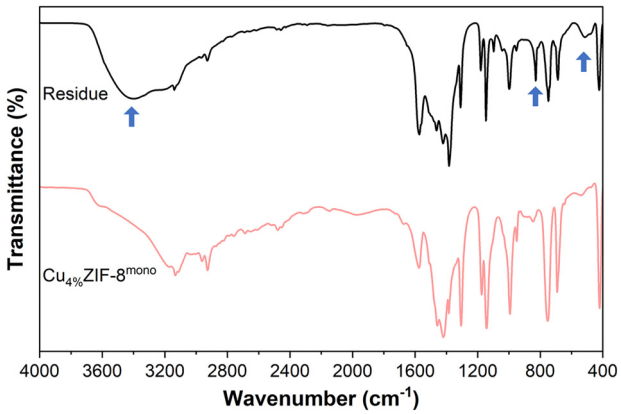

Fig. 8 FTIR spectra of the as-synthesised $Cu_{4\%}$ZIF-8^{mono} and its white residue obtained following the stability test. The blue arrows indicate the appearance of new peaks.

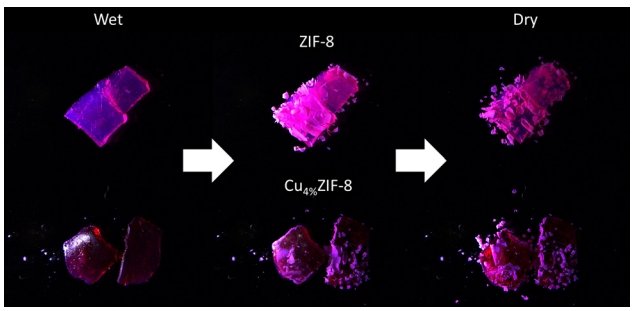

Fig. 9 Optical images of the peeling process during the drying of ZIF-8mono and $Cu_{4\%}$ZIF-8^{mono} following the RhB adsorption test.

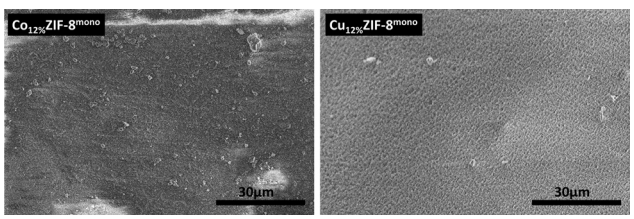

Fig. 10 SEM images of $Co_{12\%}$ZIF-8^{mono} after five days in Milli-Q water and $Cu_{12\%}$ZIF-8^{mono} after RhB adsorption.

Table 6 Compositional analysis of $Co_{12\%}$ZIF-8^{mono} following 5-day water immersion and $Cu_{12\%}$ZIF-8^{mono} post 4-day RhB adsorption and drying

	% Weight	
Element	$Co_{12\%}$ZIF-8^{mono}	$Cu_{12\%}$ZIF-8^{mono}
C	44.59	48.02
N	35.96	9.61
O	4.66	4.48
Co	3.27	—
Cu	—	1.87
Zn	11.52	36.03

The blocking of the monolith's pore after the RhB adsorption experiment was tested using N_2 adsorption. Fig. S34 shows the isotherm and the pore size distribution of ZIF-8^{mono} after the RhB adsorption experiment. The figure demonstrates that

the monolith does not get blocked and it retains its adsorption capabilities and pore size distribution after the RhB experiments. This is not a surprise since most of RhB gets desorbed after four days and most of the remaining RhB on the surface is removed by the peeling effect, which also renews the surface of the monolith.

Discussion

Since its publication in 2006, ZIF-8 has been regarded as one of the most stable MOFs in aqueous environments which has significantly promoted its use in water-purification processes.[6,20,36] One notable application is the adsorption of large dye molecules like RhB whose molecular size (13.1 × 5.5 × 1.8 Å) far exceeds the window size (3.4 Å) of ZIF-8.[26,37] However, most of the reports fail to discuss about its practical limitations – including its ability to absorb large molecules and its actual stability in water – in order to emphasise its applicability and performance in water-purification processes.

Similarly, since the first sol–gel monolithic MOF was published a decade ago, researchers have primarily focused on leveraging its properties to demonstrate its applicability and performance across various industries.[11,12,14,22,38,39] However, the limitations of these materials have often been downplayed. For instance, Mehta *et al.* have highlighted the successful photodegradation of MB using a monolithic ZIF-8 structure embedded with SnO_2.[22] Although the degradation of the monolith is reported, the stability was assessed solely through PXRD and BET. The authors omitted UV-vis analysis of the post-experiment solution in the UV region. Analysing the solution is essential, because a constant increase in the concentration of mIm would indicate monolith degradation. This degradation would undermine the practical application of the monolith since one pollutant would merely be substituted for another. Therefore, it is essential to thoroughly evaluate the adsorption capabilities of ZIF-8 monoliths in water. Consequently, here we address two important limitations of sol–gel monolithic ZIF-8: its capacity adsorption of large dyes and the stability of water.

The opening phrase of this article's title – "Size Matters" – refers to the critical role of the adsorbate's size relative to the adsorbent and its pore dimension. While previous studies on RhB adsorption in ZIF-8 have focused exclusively on nanoparticles or micro-sized particles where the particle size greatly influences dye adsorption,[24,26,37,40,41] this work investigates monolith pieces of varied sizes (from mm to cm) and shapes. This larger format exhibits significantly different absorption behaviour than their micro and nano-sized counterparts. This discrepancy arises because large molecules, such as RhB, are unable to access the small micropores of ZIF-8, restricting the adsorption primarily to the external surface. Due to their reduced external surface area, ZIF-8 monoliths present lower adsorption capacities for RhB (0.61–1.82 mg g^{-1}) than their nano- and micro-sized particles (4.1–25 mg g^{-1}).[26] This also explains the enhanced adsorption capacity of the grounded monolith, as grinding increases the external surface area. Additionally, the external surface area also affects the kinetics since the monoliths present significantly slower adsorption rates, requiring several hours to reach maximum capacity, whereas smaller particles – including the grounded monolith – achieve saturation in minutes or a couple of hours. This suggests that ZIF-8 may not be the optimal choice for adsorbing large dyes, such as RhB because monoliths, although easier to handle for industrial applications, are hindered by lower adsorption rates and capacities, while nano- and micro-sized ZIF-8 particles, which show better performance, lack the practicability for large-scale industrial applications.

The main limitation for the application of ZIF-8 in water purification is its stability. Our stability study demonstrates that water damages the external surface of the monoliths, either by forming a white residue on the external surface or by deteriorating the outer layer of the sample, which subsequently detaches upon drying. We hypothesise that this surface damage affects the adsorption of the dye due to a competitive interplay between dye uptake and monolith degradation. Initially, water-induced damage may expose additional adsorption sites for RhB. However, after six to nine hours, the degradation of the monolith's surface may become significant enough to cause substantial desorption of RhB, which lies mostly at the external surface. At this point, the remaining RhB and ZIF-8 of the external surface, together with water molecules, form a loosely bound external layer, which eventually peels off upon drying. While this layer might mitigate the degradation of the monoliths, it does not halt it entirely – evidence by the UV-vis data showing a continued, albeit reduced, increase of mIm concentration after 24 h of contact time.

The above-mentioned interplay between water-induced degradation and dye uptake may also explain the enhanced adsorption observed in Co-doped monoliths. Given that the water stability of ZIF-8 diminishes with increasing Co-doping levels, as previously reported,[42,43] monoliths with higher cobalt concentrations also exhibit greater surface damage. This damage exposes additional adsorption sites for RhB, resulting in a dynamic equilibrium where the rate of RhB adsorbed balances the desorption caused by water-induced degradation.

It is important to recognise that the water stability test relies on the analysis of post-experiment solutions using UV-Vis spectroscopy. As previously pointed out by Taheri *et al.*, "UV-vis spectroscopy is the most sensitive method to identify ZIF-8 degradation".[43] Therefore, we strongly recommend that researchers analyse the water in which the MOF is placed, showing either the liberation or absence of the MOF ligand, thereby validating the material's water stability. Analysis methods such as FTIR, SEM and XRD of the MOF post-experiment are insufficient to confirm water stability.

The doping of ZIF-8 with Ni^{2+}, Co^{2+} and Cu^{2+} ions significantly alters the properties of the monoliths. The most notable changes are observed in pore size and surface area. Doping monolithic ZIF-8, in most cases, results in a narrower pore size distribution with maximum size between 10.9 and 11.6 Å, in contrast to the wider distribution, including micropores and mesopores, observed in the undoped material. Doping also increases the BET surface area when Cu^{2+} and Co^{2+} are used as dopants.

Water stability is another property affected by the doping of the monoliths. The results of this work show that while increasing cobalt content reduces the stability, copper doping slightly improves it. Nevertheless, even with the enhanced stability provided by Cu-doping, the degradation is not entirely prevented. These results suggest that the ZIF-8 monolith and its doped variants perform poorly in water separation processes, but they show significant potential for applications in gas storage and separation.

The ZIF-8 monolith and its doped derivatives, while unsuitable for water purification, show potential as humidity sensors when loaded with RhB. The loaded monoliths exhibit a clear colour contrast between wet and dry (peeling off) states, enabling straightforward visual detection. This makes the RhB-loaded monoliths particularly useful in environments where high humidity must be maintained, as a sharp decrease in humidity can be easily identified through visual inspection.

It is worth nothing that this study has several limitations that must be acknowledged. First, our analysis focused solely on the monoliths synthesised using the recipe provided in the Experimental section. However, the impact of unwashed reactants, centrifugation speed and drying conditions on the water stability and properties of the monoliths remains unexplored. Second, the effects of pH, concentration, and size of the adsorbed dye have not been explored in this work and will be addressed in a future publication. Finally, the water stability mechanism requires further investigation, particularly regarding the quantification of the leaching metal ions. As such, the proposed mechanism should be interpreted with caution until these aspects are clarified.

Conclusions

ZIF-8 has been extensively used for the adsorption of large molecules in water. However, here we conclude that ZIF-8 is neither a good adsorbent for large molecules nor stable in water. Our attempts to adsorb RhB from 10 mg L^{-1} aqueous solutions using monolithic ZIF-8 and its Ni-, Co- and Cu-variants yielded poor results. The maximum absorption capacities ranging between 0.61 and 1.82 mg g^{-1} are significantly lower than those found in the literature. The adsorption process is also notably slow, taking several hours compared to minutes for nanoparticles and a couple of hours for microsize particles. Desorption of RhB was detected between 9 and 24 h due to monolith degradation. Poor water stability was observed by analysing the RhB solution in which the monoliths were immersed, detecting degradation up to 20%. Moreover, when immersed in pure water for five days, the monoliths developed a white residue on the surface. FTIR analysis of this residue indicates the formation of a new phase. Interestingly, PXRD analysis of the monoliths post-immersion, including their white residue, failed to detect this phase, demonstrating the inefficacy of PXRD for evaluating the water stability of these materials.

Doping the ZIF-8 monolith with Ni^{2+}, Co^{2+} and Cu^{2+} does not significantly enhance the adsorption of RhB, but it greatly alters the monolith properties. High levels of Co^{2+} lead to poor water stability. Except for the 4% Co-doped variant, doping generally narrows the pore size distribution to micropores, with a maximum between 10.9 and 11.6 Å. Contrarily, the undoped monolith has a combination of micropores and mesopores ranging from 10.2 to 38 Å. Doping with more than 4% of Co^{2+} or Cu^{2+} results in higher BET surfaces areas (1178.17 and 1099.57 m^2 g^{-1}, respectively) compared to the undoped monolith (963.58 m^2 g^{-1}). Therefore, we recommend the use of ZIF-8 and its doped variants for the adsorption of small molecules, such as gases. Their application in gas storage and separation would be significantly more suitable than the application of adsorbing large molecules in water.

Author contributions

JJVG: conceptualisation, data curation, formal analysis, investigation, supervision, writing-original draft, review and editing. SF: supervision. LSV: investigation, supervision. CHWB: resources, CC: investigation. JS: investigation. SK: investigation. TFK: resources and review. HSC: investigation. DHQ: investigation. MA: investigation. RE: investigation. LMAH: investigation. WŁ: investigation. NE: investigation. DE: investigation. ST: funding acquisition, resources, supervision.

Conflicts of interest

There are no conflicts to declare.

Data availability

The authors declare that data supporting the findings of this study are available within the paper and its supplementary information (SI). Supplementary information is available. See DOI: **https://doi.org/10.1039/d5ma00797f**.

Acknowledgements

The work in Peru was supported by a Collaboration Agreement between the Universidad Nacional Autonoma de Huanta (Peru) and the University of Cambridge (UK), Contract Number G117323. H. Sanchez thanks the Peruvian Agency CONCYTEC for financial support through grant No. PE501088281-2024-PROCIENCIA. Parts of this research were carried out at the DESY NanoLab at DESY, a member of the Helmholtz Association HGF. We are grateful to the DFG for the financial support provided for project C04/SFB 1633 ''Proto-coupled electron transfer''. HG-recruitment, HG-Innovation ''FISCOV'' and ''FISVIR'' and the CMWS are also thanked for financial support. Additionally, we are grateful to the BlueMAT for their financial contribution. LMAH and WŁ acknowledge the DESY-Helmholtz-summer student fund for financial support. We acknowledge Prof. Ashlee J. Howarth for providing access to the instrumentation for conducting the N_2 adsorption measurements in this study. We also thank the Zentrale Element-Analytik at the University of Hamburg, Germany, for performing the ICP-OES analysis. We are grateful to Christos Bintas and Edwige

N. Pujol for providing the images that accompany the synthesis instructions in the SI.

References

1 H. Furukawa, K. E. Cordova, M. O'Keeffe and O. M. Yaghi, *Science*, 2013, **341**, 1230444.
2 T. Jia, Y. Gu and F. Li, *J. Environ. Chem. Eng.*, 2022, **10**, 108300.
3 Q. Wang and D. Astruc, *Chem. Rev.*, 2020, **120**, 1438–1511.
4 H.-C. Zhou, J. R. Long and O. M. Yaghi, *Chem. Rev.*, 2012, **112**, 673–674.
5 H.-C. Joe Zhou and S. Kitagawa, *Chem. Soc. Rev.*, 2014, **43**, 5415–5418.
6 K. S. Park, Z. Ni, A. P. Côté, J. Y. Choi, R. Huang, F. J. Uribe-Romo, H. K. Chae, M. O'Keeffe and O. M. Yaghi, *Proc. Natl. Acad. Sci. U. S. A.*, 2006, **103**, 10186–10191.
7 D. Fairen-Jimenez, S. A. Moggach, M. T. Wharmby, P. A. Wright, S. Parsons and T. Düren, *J. Am. Chem. Soc.*, 2011, **133**, 8900–8902.
8 D. Fairen-Jimenez, R. Galvelis, A. Torrisi, A. D. Gellan, M. T. Wharmby, P. A. Wright, C. Mellot-Draznieks and T. Düren, *Dalton Trans.*, 2012, **41**, 10752.
9 C. O. Ania, E. García-Pérez, M. Haro, J. J. Gutiérrez-Sevillano, T. Valdés-Solís, J. B. Parra and S. Calero, *J. Phys. Chem. Lett.*, 2012, **3**, 1159–1164.
10 L. Zhang, Z. Hu and J. Jiang, *J. Am. Chem. Soc.*, 2013, **135**, 3722–3728.
11 T. Tian, J. Velazquez-Garcia, T. D. Bennett and D. Fairen-Jimenez, *J. Mater. Chem. A*, 2015, **3**, 2999–3005.
12 B. M. Connolly, D. G. Madden, A. E. H. Wheatley and D. Fairen-Jimenez, *J. Am. Chem. Soc.*, 2020, **142**, 8541–8549.
13 A. Pathak, L. A. Alghamdi, J. Fernández-Catalá, M. Tricarico, D. Cazorla-Amorós, J. Tan, Á. Berenguer-Murcia, G. Mehlana and A. E. H. Wheatley, *Small*, 2025, **21**, 2500510.
14 T. Tian, Z. Zeng, D. Vulpe, M. E. Casco, G. Divitini, P. A. Midgley, J. Silvestre-Albero, J.-C. Tan, P. Z. Moghadam and D. Fairen-Jimenez, *Nat. Mater.*, 2018, **17**, 174–179.
15 B. M. Connolly, M. Aragones-Anglada, J. Gandara-Loe, N. A. Danaf, D. C. Lamb, J. P. Mehta, D. Vulpe, S. Wuttke, J. Silvestre-Albero, P. Z. Moghadam, A. E. H. Wheatley and D. Fairen-Jimenez, *Nat. Commun.*, 2019, **10**, 2345.
16 S. Fan, Z. Chen, Z. Yang, J. Feng, L. Yu, Z. Qiu, W. Liu, B. Li and S. Zhang, *AIChE J.*, 2022, **68**, e17872.
17 C. Çamur, R. Babu, J. A. Suárez Del Pino, N. Rampal, J. Pérez-Carvajal, P. Hügenell, S. Ernst, J. Silvestre-Albero, I. Imaz, D. G. Madden, D. Maspoch and D. Fairen-Jimenez, *Adv. Mater.*, 2023, **35**, 2209104.
18 L. G. Marazani, V. Gascon-Perez, A. Pathak, M. Tricarico, J.-C. Tan, M. J. Zaworotko, A. E. H. Wheatley, B. C. E. Makhubela and G. Mehlana, *Mater. Adv.*, 2024, **5**, 7679–7689.
19 E. Hunter-Sellars, P. A. Saenz-Cavazos, A. R. Houghton, S. R. McIntyre, I. P. Parkin and D. R. Williams, *Adv. Funct. Mater.*, 2021, **31**, 2008357.
20 A. Elaouni, M. El Ouardi, M. Zbair, A. BaQais, M. Saadi and H. Ait Ahsaine, *RSC Adv.*, 2022, **12**, 31801–31817.
21 U. Ahmad, S. Ullah, A. Rehman, T. Najam, S. S. Alarfaji, M. Jamshaid, O. Parkash Kumar, S. Ullah, M. Shahid, S. S. Ahmad Shah and M. Altaf Nazir, *ChemistrySelect*, 2024, **9**, e202401719.
22 J. P. Mehta, T. Tian, Z. Zeng, G. Divitini, B. M. Connolly, P. A. Midgley, J. Tan, D. Fairen-Jimenez and A. E. H. Wheatley, *Adv. Funct. Mater.*, 2018, **28**, 1705588.
23 H. Yang, S. Hu, H. Zhao, X. Luo, Y. Liu, C. Deng, Y. Yu, T. Hu, S. Shan, Y. Zhi, H. Su and L. Jiang, *J. Hazard. Mater.*, 2021, **416**, 126046.
24 M. Chin, C. Cisneros, S. M. Araiza, K. M. Vargas, K. M. Ishihara and F. Tian, *RSC Adv.*, 2018, **8**, 26987–26997.
25 H. Zhang, M. Zhao and Y. S. Lin, *Microporous Mesoporous Mater.*, 2019, **279**, 201–210.
26 B. Luan Tran, H.-Y. Chin, B. K. Chang and A. S. T. Chiang, *Microporous Mesoporous Mater.*, 2019, **277**, 149–153.
27 A. Stierle, T. F. Keller, H. Noei, V. Vonk and R. Roehlsberger, *JLSRF*, 2016, **2**, A76.
28 H. Yuh-Shan, *Scientometrics*, 2004, **59**, 171–177.
29 Y. Feng, Y. Li, M. Xu, S. Liu and J. Yao, *RSC Adv.*, 2016, **6**, 109608–109612.
30 X. He, K. B. Male, P. N. Nesterenko, D. Brabazon, B. Paull and J. H. T. Luong, *ACS Appl. Mater. Interfaces*, 2013, **5**, 8796–8804.
31 Y. S. Ho and G. McKay, *Process Biochem.*, 1999, **34**, 451–465.
32 W. Plazinski and W. Rudzinski, *J. Phys. Chem. C*, 2009, **113**, 12495–12501.
33 M. Ahmad, R. Patel, D. T. Lee, P. Corkery, A. Kraetz, Prerna, S. A. Tenney, D. Nykypanchuk, X. Tong, J. I. Siepmann, M. Tsapatsis and J. A. Boscoboinik, *ACS Appl. Mater. Interfaces*, 2024, **16**, 27887–27897.
34 R. Li, X. Ren, H. Ma, X. Feng, Z. Lin, X. Li, C. Hu and B. Wang, *J. Mater. Chem. A*, 2014, **2**, 5724–5729.
35 C. Zhang, J. A. Gee, D. S. Sholl and R. P. Lively, *J. Phys. Chem. C*, 2014, **118**, 20727–20733.
36 Z. Mo, D. Tai, H. Zhang and A. Shahab, *Chem. Eng. J.*, 2022, **443**, 136320.
37 X. Fan, W. Wang, W. Li, J. Zhou, B. Wang, J. Zheng and X. Li, *ACS Appl. Mater. Interfaces*, 2014, **6**, 14994–14999.
38 D. G. Madden, R. Babu, C. Çamur, N. Rampal, J. Silvestre-Albero, T. Curtin and D. Fairen-Jimenez, *Faraday Discuss.*, 2021, **231**, 51–65.
39 D. G. Madden, D. O'Nolan, N. Rampal, R. Babu, C. Çamur, A. N. Al Shakhs, S.-Y. Zhang, G. A. Rance, J. Perez, N. P. Maria Casati, C. Cuadrado-Collados, D. O'Sullivan, N. P. Rice, T. Gennett, P. Parilla, S. Shulda, K. E. Hurst, V. Stavila, M. D. Allendorf, J. Silvestre-Albero, A. C. Forse, N. R. Champness, K. W. Chapman and D. Fairen-Jimenez, *J. Am. Chem. Soc.*, 2022, **144**, 13729–13739.
40 Y. Li, K. Zhou, M. He and J. Yao, *Microporous Mesoporous Mater.*, 2016, **234**, 287–292.
41 M. A. Nazir, T. Najam, K. Shahzad, M. A. Wattoo, T. Hussain, M. K. Tufail, S. S. A. Shah and A. U. Rehman, *Surf Interfaces*, 2022, **34**, 102324.
42 D. Saliba, M. Ammar, M. Rammal, M. Al-Ghoul and M. Hmadeh, *J. Am. Chem. Soc.*, 2018, **140**, 1812–1823.
43 M. Taheri, T. G. Enge and T. Tsuzuki, *Mater. Today Chem.*, 2020, **16**, 100231.